A Method for Quantitative Imaging of Electrical Properties of Human Tissues from Only Amplitude Electromagnetic Data

Martina T. Bevacqua [1], Gennaro G. Bellizzi [1,2], Lorenzo Crocco [1,2] and Tommaso Isernia[1,2]

[1] DIIES, Department of Information Engineering, Infrastructures and Sustainable Energy, Università Mediterranea di Reggio Calabria, DIIES Dept., via Graziella, Loc. Feo di Vito, 89124, Reggio di Calabria, Italy.
[2] CNR-IREA, National Research Council of Italy – Institute for Electromagnetic Sensing of the Environment, via Diocleziano 328, 80124, Napoli, Italy.

Abstract

The estimation of electrical properties of living biological tissues is relevant to several medical applications ranging from hyperthermia treatment planning to dosimetry and, more in general, is pivotal for a fundamental understanding of bioelectromagnetic interactions. Non-invasive electromagnetic imaging, either based on the processing of electric fields measured via microwave tomography or magnetic fields acquired in magnetic resonance is suitable to pursue this goal. In this framework, the possibility of imaging without the need of phase information would be extremely relevant, as it would enable simpler and more reliable devices and would avoid limiting assumptions typically used in the literature. To this end, in this paper, we propose an inverse scattering approach for tissue characterization from only-amplitude electromagnetic data, which is viable for both microwave tomography and magnetic resonance imaging, thanks to a unified mathematical framework herein introduced. The key feature of the method is the innovative use of morphological maps derived by other medical imaging modalities as prior spatial information. In particular, these images are exploited to define a convenient and effective patient-specific representation of the unknowns. The approach is tested against simulated data in case of realistic and anthropomorphic head and pelvis phantoms.

Keywords: contrast source inversion, electrical properties, electromagnetic inverse scattering, image reconstruction, inverse methods, magnetic resonance imaging, microwave imaging, segmentation, B_1^+ map, phaseless measurements.

Submitted to: *Inverse Problems*

1. Introduction

The knowledge of the electrical properties (EPs), namely conductivity and permittivity, of living biological tissues has an intrinsic interest for its relevance in different biomedical applications. EPs are indeed fundamental in hyperthermia treatment planning [1-3] and electromagnetic dosimetry [4], as the accuracy of the assumed electrical model plays a key role on actual performances of the treatment and on the proper

evaluation of field exposure. Moreover, EPs are also relevant for diagnostic purposes and can give rise to unconventional check-up and follow-up techniques. Indeed, the values of EPs can be related to the health condition of biological tissues so that anomalies with respect to expected reference values may represent a warning about pathologies.

Nowadays, the EPs values are derived from ex-vivo measurements. For instance, virtual patients for bio-electromagnetic applications are developed starting from the tissue anatomy derived by segmented magnetic resonance imaging (MRI) or computed tomography (CT) images, and by associating to each tissue the EPs taken from existing databases wherein such ex-vivo measurements are collected [5]. However, the agreement between the EPs measured ex-vivo and the in-vivo values of living tissue still represents an open problem and some recent papers have shown that a difference between the ex-vivo and in-vivo EPs exists [6].

As a consequence, several studies have been focused on the development of non-invasive techniques to retrieve EPs in-vivo, directly in the human body. To this end, one possibility is given by a recently introduced imaging modality based on a proper processing of the magnetic field acquired by an MRI system [7]. This technique can reach a spatial resolution of the order of a few millimeters and high accuracy in determining the electrical parameters of the scenario. However, this mapping can be performed only at the resonance frequency of the MRI apparatus. As a consequence, a dispersion relation (to extrapolate data from the MRI Larmor frequency to the ones of interest) is needed. In addition to this, the measured data are affected by phase uncertainties. Indeed, while various methods have been proposed to measure the magnitude of B_1^+ map, there is no way to quantitatively measure the absolute phase. To cope with this issue, the so-called transceiver phase assumption is usually adopted [8-10]. However, this assumption holds true just in case of MR systems with a quadrature body coil and is more effective for lower-field MRI and on regions with lower permittivity and symmetric structure [11]. Therefore, MRI based EPs retrieval should rely on a procedure able to deal with phaseless data.

As an alternative, microwave tomography (MWT) [12] can be exploited to image EPs. As a matter of fact, MWT provides a low-cost and non-invasive modality to investigate the human body in a whole spectrum of frequencies of interest. On the other hand, as compared to MRI and CT, MWT exhibits a low spatial resolution, which may ultimately impair the creation of reliable and accurate electrical models. In addition, although phase measurements are of course possible at microwave frequencies, also MWT can take a remarkable advantage from only amplitude data, in terms of a significant reduction of the complexity (and cost) of the required hardware. In particular, simpler MWT devices are more easily integrable within existing clinical systems, such as hyperthermia applicators and MRI machines. For instance, clinical systems already

adopted for microwave hyperthermia treatment, such as [1], could be enhanced with the capability of performing, without significant modifications, a pre-treatment patient-specific estimation of the electromagnetic scenario at the exact frequency of interest. Finally, the possible exploitation of minimally-invasive only-amplitude probes [13] would yield to a higher MRI compatibility of microwave system, thus allowing a simultaneous acquisition of MRI and microwave signals.

Accordingly, both MRI and MWT are potential candidates for EPS mapping of living tissues, but they would both take great advantage from the chance of using only-amplitude data to adopt devices simpler as possible. However, both these modalities involve the solution of a non-linear and ill-posed inverse problem, whose difficulties indeed significantly worsen when phase measurements are not available or cannot be performed [14].

With respect to this framework, this paper explores the possibility of estimating EPs using phaseless electromagnetic data, by relying on a regularization by projection technique, which benefits from the tissue segmentation extracted from MRI or CT. More in detail, the available spatial priors are exploited to build a *patient-specific* representation basis of the unknown EPs, which are then encoded by means of a set of (complex) coefficients. By so doing, the anatomical information is exploited to achieve a significant reduction of the number of unknowns, which allows to mitigate or even overcome the unavoidable loss of information associated with only-amplitude measurements. Notably, there is no restriction on the number of tissues, nor assumptions on some tissues or the need of selecting any regularization parameter.

In the following, the approach is assessed with both the case of phaseless MWT, in which the sole amplitude of the electric total field is measured, and the case of EPs estimation from phaseless B_1^+ data acquired by an MRI scanner. In such a context, we unprecedentedly set both tomographic techniques under a common mathematical framework and estimate the biological EPs by incorporating the introduced *patient-specific* representation basis into a phaseless contrast source inversion method (CSI) [14,15]. It is important to remark that the adopted regularization via projection scheme belongs to the class of *hard* prior techniques as it relies on the approximation of the actual EPs distributions with a step-wise constant distribution. This is not a limitation as it is the common assumption in therapeutic treatments or dosimetry [1,4]. Moreover, *hard* prior techniques, compared with the "antagonistic" *soft* prior ones, have shown better capability in retrieving the biological EPs [16].

To the best of our knowledge, the only available example of phaseless EPs retrieval is the very recent work by Arduino et al. [17], wherein a CSI scheme is also exploited for phaseless MRI based tomography. However, in this work, the additional under-determination of the inverse problem arising

from only amplitude data is faced assuming that an MRI device with multiple independent transmit/receive channels is used. Thanks to the adopted *patient-specific* representation basis, the approach herein proposed can instead work with a single transmitter MRI system, with an obvious advantage in terms of scan time, which plays a pivotal role in the clinic.

More in general, as far as the idea of integrating MRI or CT spatial priors into EPs tomography (with phase and amplitude data) is concerned, there are several interesting contributions in the literature [16,18-20]. However, these works consider non-realistic and over-simplified anatomical scenarios. Also, there are several significant differences between the method herein proposed and those studies, as explained in the following.

In particular, in [16,18,19] the EPs retrieval via MWT has been tackled by using both amplitude and phase data and enforcing the spatial priors as penalty terms within a l_2 norm regularization framework. This latter circumstance entails the need of weighting their contribution through properly selected parameters, which is not a trivial issue in non-linear inverse problem and may significantly affect the ultimate solution. Moreover, the conceptual and computational complexity of the regularization strategy makes the approach not viable for (realistic) scenarios where more than a few tissues are present.

The approach introduced in [20] for EP tomography from MRI data is also based on the processing of both amplitude and phase (of B_1^+ map). Also, it arbitrarily assumes some tissues in the segmented region to be exactly known, which is not the case in our approach. Moreover, constrains are used to ensure positive permittivity and conductivity estimations, which may does not necessarily positively affect the convergence of the optimization task. Last, the inversion scheme adopted in [20] belongs to the class of Newton-Kantorovich methods. These inversion schemes require the solution of several forward problems to compute adjoint fields, which is a computationally demanding task. Notably, this is not the case for CSI based inversion herein adopted, wherein the forward problem is solved in an implicit fashion throughout the minimization.

The paper is organized as follows. In Section II, the unified mathematical formulation for the EPs retrieval problem using either MWT or MRI phaseless data is given, by emphasizing common aspects and relevant differences. In Section III, the proposed regularization by projection is introduced and described, while section IV considers its integration into a phaseless CSI scheme. In Section V, an extensive numerical analysis against realistic and anthropomorphic scenarios is reported. Also, a comparison with the performance obtained with the usual pixel representation is given. Finally, Conclusions follow.

Throughout the paper we assume and drop the time harmonic factor $exp\{j\omega t\}$ and we consider the canonical 2D scalar problem (TM polarized fields).

2. MWT and MRI based Tomography

Let us encode the EPs of the tissues under investigation through the contrast function $\chi(\boldsymbol{r}) = \epsilon_s(\boldsymbol{r})/\epsilon_b(\boldsymbol{r}) - 1$, being ϵ_s and ϵ_b respectively the complex permittivities of the tissues and the coupling medium, with $\boldsymbol{r} = (x, y)$ being a generic point in the imaged domain Ω. In the case of an MRI scanner, the coupling medium is air (the radiofrequency shield is not taken into account in our model). In MWT, the human tissues are typically coupled with the antennas by means of a matching medium of permittivity ϵ_b, in order to maximize the amount of incident power that penetrates into them.

In case of phaseless data, EPs mapping via MWT or MRI data can be described by the unified formulation given by the following pair of equations [8,12]:

$$M_t^2(\boldsymbol{r_r}, \nu) = |\mathcal{A}[W(\boldsymbol{r}, \nu)] + F_i(\boldsymbol{r_r}, \nu)|^2$$

(1)

$$W(\boldsymbol{r}, \nu) = \chi E_i(\boldsymbol{r}, \nu) + \chi \mathcal{A}_i[W(\boldsymbol{r}, \nu)]$$

(2)

wherein:

- $M_t^2 = \begin{cases} |E_t|^2 & \text{in MWT} \\ |B_{1,t}^+|^2 & \text{in MRI} \end{cases}$
- $F_i = \begin{cases} E_i & \text{in MWT} \\ B_{1,i}^+ & \text{in MRI} \end{cases}$
- $\boldsymbol{r_r}$ is the position where the electromagnetic data are measured;
- ν identifies the different illumination (transmitter) conditions;
- W is the electric current distribution induced in the imaged domain Ω.

The electric currents are induced by the radiofrequency (complex) incident electric field $\boldsymbol{E_i}(\boldsymbol{r}, \nu) = E_i(\boldsymbol{r}, \nu) \, \hat{\boldsymbol{z}}$, coupled to a magnetic field $\boldsymbol{B_i}(\boldsymbol{r}, \nu) = B_i^x(\boldsymbol{r}, \nu) \, \hat{\boldsymbol{x}} + B_i^y(\boldsymbol{r}, \nu) \, \hat{\boldsymbol{y}}$ and generated in the region Ω when the patient is not present. The incident field is generated by microwave antennas in the MWT case and by the coils in the MRI scanner.

The problem's data are given by M_t^2. In MWT, this quantity denotes the square amplitude of the measured (total) electric field $E_t(\boldsymbol{r_r}, \nu)$. On the contrary, in MRI based tomography, the useful signal is represented by the positively circularly polarized component of the radiofrequency magnetic field, which rotates as the nuclear Larmor precession. In particular, M_t^2 represents the square amplitude of the measured (total) transmit sensitivity, which is defined as $B_{1,t}^+ = \frac{1}{2}(B_{1,t}^x + jB_{1,t}^y)$. An important difference between the two cases resides in the position where the data are measured. In MWT, receiving antennas are located on a closed curve Γ external to the region Ω, while MRI data are directly available inside the inspected body. This represents a crucial difference as a much larger amount of data is available in the MRI case.

$\mathcal{A}$ and $\mathcal{A}_i$ are a short notation for the linear integral radiation operators which are defined on $S \subset L^2(\Omega)$ a proper subspace for the contrast sources, and with value on two proper subspaces for the scattered fields outside or inside the object, $S_e \subset L^2(\Gamma)$ and $S_i \subset L^2(\Omega)$. In particular, when dealing with MWT, the operator $\mathcal{A}$ relates the electric currents induced in Ω to electric field measured on Γ. From a mathematical point of view, it is defined as [12]:

$$\mathcal{A}[W(\boldsymbol{r},v)] = \int_\Omega G_b(\boldsymbol{r_r},\boldsymbol{r'}) \, W(\boldsymbol{r'},v) d\boldsymbol{r'}$$

(3)

where G_b is the Green's function pertaining to the background medium and $\boldsymbol{r_r} \in \Gamma$. In MRI based tomography, the operator $\mathcal{A}$ relates the electric currents induced in Ω to magnetic fields $B_{1,t}^+$ measured in Ω and is defined as [10]:

$$\mathcal{A}[W(\boldsymbol{r},v)] = -\frac{k_b^2}{2j\omega}(\partial_y - j\partial_x) \int_\Omega G_b(\boldsymbol{r_r},\boldsymbol{r'}) \, W(\boldsymbol{r'},v) d\boldsymbol{r'}$$

(4)

wherein $\boldsymbol{r_r} \in \Omega$. Finally, in both cases, $\mathcal{A}_i$ relates the contrast source W in Ω to the electric scattered field in Ω and is defined as [8,12]:

$$\mathcal{A}_i[W(\boldsymbol{r},\boldsymbol{v})] = k_b^2 \int_\Omega G_b(\boldsymbol{r},\boldsymbol{r'}) \, W(\boldsymbol{r'},\boldsymbol{v}) d\boldsymbol{r'}$$

(5)

MWT usually takes advantage from multiple (or multiview) experiments, i.e., from considering N_A incident fields impinging from different angles which produce a corresponding set of scattered fields ($v = 1,2,\dots,N_A$). Note that, when considering only-amplitude data, the number of data samples, required to correctly collect all the available information, becomes four times larger with respect to the case of both amplitude and phase measurements [14]. As a consequence, a large value of N_A would have to be considered. Luckily, the regularization strategy, proposed in the next Section, allows to overcome this relevant drawback.

In MRI based tomography, due to the large amount of available data, the inversion is usually performed by considering just one channel transmit coil. Recently, in order to defeat problems arising from phaseless data, approaches exploiting multiple measurements of different transmit sensitivities have been introduced [17,21]. In fact, the use of multiple independent transmit/receive channels can open up possibilities for EPs reconstruction avoiding assumptions regarding the phase1. However, as short scans are desirable in

the clinics, we assess the proposed regularization strategy for the case of just one channel transmit coil ($v = 1$).

3. Regularization via Tissue Projection

The inverse scattering problem (1)-(2) underlying both MRI based tomography and MWT is non-linear, as both the induced currents W and the contrast function χ are unknowns of the problem, and it is also ill-posed due to the properties of the involved operators [8,12].

To overcome these difficulties, a priori information on χ can be exploited [24,25]. To this end, the concept herein pursued is to exploit a representation basis conveniently derived from the segmentation of the MRI or CT images, rather than the more usual pixel basis representation. As a matter of fact, this segmented basis allows to reduce the dimensionality of the unknown space and avoid the occurrence of false solutions [26].

Let N be the number of tissues arising from the MRI image segmentation. Then, a *tissue space* for the segmented biological scenario is introduced as the set of tissue basis functions $\{\mathcal{T}_n\}_{n=1}^N$, such that the generic function $\mathcal{T}_n$ is different from zero in all pixels associated with the n-th tissue and zero elsewhere. Note the functions $\mathcal{T}_n$ are not required to identify regions of Ω simply connected, namely they can also represent the union of more disjoint non-empty subsets. Accordingly, the contrast function χ can be conveniently projected into this space, i.e.:

$$\chi(r) = \sum_{n=1}^N \hat{\chi}_n \, \mathcal{T}_n(r) = \mathcal{T}(\hat{\chi})$$

(6)

where $\mathcal{T}$ is the operator which works on the coefficients and returns a pixel representation.

By using representation (6) in the solution of the inverse scattering problem (1)-(2), the actual unknowns of the problem become the coefficients $\hat{\chi} = \{\hat{\chi}_n\}_{n=1}^N$, which represent the effective EPs corresponding to the n-th tissue. The problem is hence reduced to a parameter estimation problem, wherein only a single (complex) coefficient $\hat{\chi}_n$ is looked for in each tissue. By doing so, the number of unknown parameters is reduced to N and a strong reduction of the ill-posedness and of the difficulties related to non-linearity is achieved [26]. Consequently, the representation (6) could allow to process a number of independent data smaller or even much smaller than the one usually required in phaseless imaging or, for a fixed number of data, to retrieve more accurate EPs maps, as shown in the numerical section.

---

1 Modern clinical MRI systems are often equipped with independent multi-transmit system primarily for RF shimming purposes [22,23].

Moreover, unlike approaches in [16,18,19], the proposed regularization procedure has a high flexibility to deal with heterogeneous and realistic anthropomorphic scenarios made up of many tissues, and there is no need of selecting any regularization parameter.

Note that the tissue projection (6) represents a general approach to deal with in-vivo estimation of patient-specific EPs and it can be used in conjunction with different assessed inversion techniques. The very low number of parameters one is looking for would even enable a fruitful exploitation of global optimization techniques. However, this interesting possibility entails the solution of several forward problems, which are computationally demanding especially in 3D geometries. For this reason, in the following, the regularization via tissue projection (6) is included in a phaseless CSI scheme [14,15]. Such an approach, being based on the joint minimization of both the state and the data equation, does not require the solution of the forward problem at each step of the iterative procedure, which is indeed implicitly taken into account, as described in the next Section.

4. Phaseless Contrast Source Inversion

The CSI method tackles the problem in its full non-linearity by simultaneously looking for both the contrast χ and the contrast sources W, which is considered as an *auxiliary* unknowns. In particular, the problem's solution is iteratively built by minimizing a non quadratic cost functional, which exhibits many different local minima corresponding to false solutions of the problem [26]. This circumstance gets worse when only phaseless measurements are available, as the case at hand [14].

To perform the optimization task underlying CSI, local (gradient-based) minimization schemes are usually adopted. However, these latter only converge to the closest local minimum of the cost functional, unless proper regularization tools are introduced. In order to prevent such a drawback, the regularization via tissue projection (6) is embedded in the minimization of the underlying cost functional, i.e.:

$$\Phi(\hat{\chi}, W) = \Phi_{S}(\hat{\chi}, W) + \Phi_{D}(W)$$

with:

$$\Phi_{S}(\hat{\chi}, W) = \sum_{\nu} \frac{\|\mathcal{T}(\hat{\chi})E_i(\nu) + \mathcal{T}(\hat{\chi})\mathcal{A}_i[W(\nu)] - W(\nu)\|^2}{\eta_{S}(\nu)}$$

$$\Phi_{D}(W) = \sum_{\nu} \frac{\|\|\mathcal{A}[W(\nu)] + F_i(\nu)|^2 - M_t^2(\nu)\|^2}{\eta_{D}(\nu)}$$

(7)

wherein the dependence from $\boldsymbol{r}$ is omitted for the sake of brevity, $\|\cdot\|$ is the ℓ_2 norm, and $\eta_{S}(\nu)$ and $\eta_{D}(\nu)$ are two normalization coefficients. In particular, η_{D} is selected equal to $\|M_t^2\|^2$, while the normalization coefficient η_{S} for the MRI case is equal to the norm of the product of the contrast function, estimated at the previous iteration of the iterative

procedure adopted to minimize (7), times the incident field. On the contrary, in MWT normalization coefficient η_{S} is the norm of the incident field. This different choice is due to the fact that in MRI based tomography the contrast function has a higher amplitude due to the presence of air as background medium, which has an impact on the speed of convergence.

It is important to underline that the functional (7) is quadratic with respect to the contrast (for any fixed W) while it is quartic with respect to the contrast sources (for any fixed contrast). This circumstance strongly motivates a joint updating of the two unknowns W and χ during the minimization of (7), differently from the usual CSI implementations [10,15].

Details about its implementation in the framework of CSI gradient-based optimization are given in the Appendix.

5. Numerical Analysis

The proposed strategy has been assessed with both MRI and MWT phaseless data. In particular, two different anatomical scenarios (the pelvis and the head) have been considered for both cases and the beneficial effect of the *tissue* representation assessed. Notably, both scenarios are clinically relevant and related to challenging anatomical districts, made up by several tissues [27,28].

5.1 Description of the numerical testbeds.

The anatomical models herein adopted have been obtained by merging the morphological information gathered from a high-resolution voxel-based anthropomorphic phantom [29] with the results from *ex-vivo* tissue dielectric spectroscopy [30]. In particular, EPs have been defined by the 4th order Cole-Cole dispersive model applied to measurements collected from IT'IS foundation database [30]. Then, on the basis of the results in [31,32], these values have been increased of about 25% for permittivity and 30% for conductivity, in order to mimic *in-vivo* EPs. Finally, to deal with a more realistic scenario (i.e., a non-exactly stepwise constant profile), EPs have been perturbed by a ±10% uniformly distributed random fluctuations.

Two different transverse slices of the above described voxel model have been considered. The first section is related to the head, enclosed within a square of side 0.22 m and a 200×200 discretization, whereas the second one refers to the low pelvis, enclosed with a square region of side 0.456 m and a 114×114 discretization. Figures 1.(a) and (d), and 2.(a) and (d) depict the permittivity and conductivity distributions of these reference profiles respectively.

The aforementioned anthropomorphic models have been tested within both imaging systems. Within the MRI scanner, the total electromagnetic fields generated by the transmit coil was calculated at 128MHz (considering a 3T scanner [8]). According to [17], the incident field radiated by the coil has been evaluated by considering a radius of 0.16 m and 0.35 m,

	Head				Pelvis			
	$\mathcal{T}_n$ *basis*		*Pixel basis*		$\mathcal{T}_n$ *basis*		*Pixel basis*	
SNR	NMSE [%]	# iter	NMSE [%]	# iter	NMSE [%]	# iter	NMSE [%]	# iter
70	0,11	732	3,83	667	0,28	1057	4,36	673
60	0,02	889	3,76	733	0,20	1227	4,30	726
50	0,12	638	8,32	1887	0,21	1175	4,40	1040
40	0,20	523	60,77	21784	0,31	1074	23,56	2982

Table I. NMSEs and number of required iterations via $\mathcal{T}_n$-CSI and pixel based CSI with MRI data.

	$\mathcal{T}_n$ *basis*				*Pixel basis*			
	N_A=44		N_A=32		N_A=44		N_A=32	
SNR	NMSE [%]	# iter	NMSE [%]	# iter	NMSE [%]	# iter	NMSE [%]	# iter
70	0,01	2939	0,01	3745	1,16	8916	1,44	7702
60	0,01	2868	0,01	3763	1,87	11534	2,33	13650
50	0,04	2292	0,03	3214	2080	92380°	548	39700°
40	0,51	1873	0,55	1492	87,55	10000°	71,36	10000°

Table II. NMSEs and number of required iterations via $\mathcal{T}_n$-CSI and pixel based CSI with MWT data for the **head** case.

	$\mathcal{T}_n$ *basis*				*Pixel basis*			
	N_A=34		N_A=20		N_A=34		N_A=20	
SNR	NMSE [%]	# iter	NMSE [%]	# iter	NMSE [%]	# iter	NMSE [%]	# iter
70	0,81	1117	0,82	1124	0,85	1339	1,16	1125
60	1,12	925	0,94	1131	0,91	1343	1,72	2192
50	1,93	743	2,64	1060	19,05	3338	95,31	8552
40	2,26	476	7,52	600	183,89	5395	431,25	10000°

Table III. NMSEs and number of required iterations via $\mathcal{T}_n$-CSI and pixel based CSI with MWT data for the **pelvis** case.

respectively for the head and the pelvis. On the other side, within the MWT system, the working frequency has been set equal to 1GHz for the head, according to [33,34], and to 128MHz for the pelvis, according to [27]. The set of incident fields radiated by N_A antennas, acting both as transmitters and receivers, are modelled as line sources and have been considered evenly spaced on a circumference of radius 0.16 m and 0.35 m respectively for the head and pelvis. In this latter case, the robustness against the reduction of the number of antennas, with respect to the one required to correctly collect all the independent information [14], has been appraised. In particular, N_A= 44 and 32 have been considered for the head, and N_A= 32 and 20 for the pelvis.

The data have been simulated by using a full-wave forward simulator based on the method of moments and corrupted with white (complex) Gaussian noise at a given SNR, accordingly to the model described in [35]. Four different level of SNR (70dB, 60dB, 50dB and 40dB) have been superimposed to the simulated total electromagnetic field data to assess the proposed approach against the measurement uncertainties.

Concerning the background medium, different media have been used for the two imaging modalities. Within the MRI scanner, air was assumed to be the background ($\epsilon_r = 1$). On the other side, into the MWT system, a medium with permittivity of 40 and conductivity of 0,01 S/m for the head [33,34], whereas water ($\epsilon_r = 78$ and $\sigma = 0,04\,S/m$) has been adopted for the pelvis, as in the case of a hyperthermia treatment [27].

Concerning the initialization of the CSI procedure, in order to reduce the computational time, the CSI procedure has been initialized by setting the coefficient $\hat{\chi}_n$ with the *ex-vivo* properties [30]. Finally, the $\mathcal{T}_n$ basis functions have been defined starting from the voxel phantom exploited to build the model [29].

The accuracy of the retrieved EPs has been appraised through the normalized mean square error (NMSE):

$$NMSE = \frac{\left\| \epsilon_{s,n} - \tilde{\epsilon}_{s,n} \right\|^2}{\left\| \epsilon_{s,n} \right\|^2}$$

(8)

where $\epsilon_{s,n}$ is the actual complex permittivity of the n-th coefficient of the adopted basis representation and $\tilde{\epsilon}_{s,n}$ is the estimated value. More in detail, in case of *tissue* representation, the error is evaluated by considering the coefficients of the N segmented tissues, while in case of *pixel* representation, the error takes into account the retrieved EPs in each pixel.

Unlike [17,20], no physical constraints have been enforced on the EPs of the investigated tissue during the minimization procedure.

5.2 Results and discussion.

Figures 3, 4 and 5 provide a pictorial representation, in terms of histograms, of the retrieved permittivity and conductivity values for both scenarios and for both MRI and MWT data, when the tissue basis representation (using $T = 7$ and 8 for the head and pelvis, respectively) is adopted. The corresponding NMSEs and the number of iterations required during the minimization procedure are reported in Tables I, II and III. Here, the superscript ° denotes those cases wherein the iterative procedure, being trapped in a false solution, is stopped without fulfilling the adopted stopping rule.

These results show the high accuracy of the proposed approach in estimating the effective EPs. As a matter of fact, NMSEs are much lower than the one corresponding to the starting guess ($\approx$5%) for both the considered scenarios. Let us note that, with respect to [20], the number of tissues considered to be unknown is higher and the whole set retrieved (without arbitrary fixing a-priori some of them). Moreover, the performances are kept approximately constant when the amount of noise superimposed on simulated data increases and when, in the case of MWT data, the number of measured data N_A is reduced.

Concerning the influence of the starting guess in the iterative CSI procedure, we have considered other initial EPs profiles without observing significant differences with respect to the ex-vivo initialization. For instance, in case of head profile and MWI from 44 antennas with SNR equal to 70 dB, the CSI procedure has been initialized by considering two different initial guesses with NMSEs equal to 46% and 100% respectively. Despite this significant difference, the procedure regularized via tissue projection converge to solutions with NMSEs equal to 0.01 and 0.005, with a number of total iterations equal to 4282 and 5601, respectively.

In order to estimate and assess the regularizing effect of the proposed approach we have compared the results gathered exploiting both the *tissue* based representation and a standard *pixel* based one. Figure 1 and 2 show the permittivity and conductivity profiles retrieved by means of phaseless CSI enhanced by both the projection into *tissue* space and into pixel one, corresponding to a SNR and 40 dB and 32 antennas, respectively. These figures, as well as the NMSEs, prove that

even if a *pixel* based representation could, in principle, allow gathering punctual information, the ill-posed and non-linear nature of the problem severely hamper reconstructions. Indeed, the corresponding NMSEs are close to the one corresponding to the starting guess, i.e., approximately 3%, for a low amount of superimposed noise, whereas the reconstruction procedure completely fails for higher noise levels. On the contrary, by exploiting the *tissue* based representation, the proposed procedure can accurately and robustly retrieve the searched EPs. Note that the starting guess in case of pixel based reconstruction is obtained by associating to each tissue a constant values corresponding to the ex-vivo EPs. Moreover, the estimation procedure has been aided providing the support of the scenario to be reconstructed, thus reducing the number of unknowns to be retrieved.

As a further proof aimed at exploring the possibility to achieve a pixel-like resolution by taking advantage from the step-wise constant reconstructions, the retrieved EPs of the brain tissues in figures 3.(b)-(c) have been assumed as starting guesses for the pixel based inversion. The NMSEs corresponding to the thus obtained profiles with SNR equal to 70 dB, 60 dB and 50 dB are respectively 0.1%, 0.09% and 2.64%, while in case of 40 dB the minimization procedure completely fails in retrieving the EPs profile. This example, and several others, show that, for high SNR the iterative inversion basically stagnates in the starting point, while for low SNR ill conditioning negatively impacts on the final result, which significantly departs from the actual solution. This further confirms the key role played by the introduced regularization via projection especially in case of inadequate SNRs.

As a final remark, it is important to take into consideration that the phaseless nature of the useful data clearly increases the overall difficulties of the problem. Moreover, the measurement configurations herein adopted in MWT consist in a lower number of antennas with respect to the actual number of degrees of freedom [14].

Finally, note that for the pelvis case within the MWT system both frequency and matching media were not optimally chosen, as instead for the head case [33,34]. This could explain the lower reconstruction accuracy found for the inner organs such as the bowel and the prostate, see Fig. 4. On the other side, the adopted matching media and frequency are consistent to clinical conditions [27].

Conclusions

In this paper, a method to perform the *in-vivo* quantitative estimation of effective EPs of biological tissues from only-amplitude electromagnetic data has been presented. Notably, thanks to unified mathematical framework herein introduced, the proposed approach can process data acquired either inside an MRI scanner or an MWT system. Moreover, it benefits from anatomical information derived from more usual medical

images, namely MRI or CT, which is incorporated inside a phaseless CSI scheme. In particular, different from other approaches in literature, this spatial prior is exploited to enable a low-order representation of the unknown, which is crucial to successfully cope with the additional difficulties arising from the lack of phase information.

As shown in the numerical analysis, the method exhibits high flexibility and applicability, as well as high accuracy in the determination of the EPs. Its performances have been assessed and evaluated against a 2D realistic and anthropomorphic head and pelvis scenarios and an extensive analysis has been performed by varying the amount of noise on the data and, for the MWT case, the number of antennas. Notably, unlike [17,21], in this paper, only a one channel coil is considered for the MRI based case.

An important aspect, which derives from the unified formulation herein given for the two imaging modalities, is the perspective of a combined imaging approach, in which data are acquired with both MRI coil and microwave antennas. Notably, such a possibility is readily implementable within the proposed inversion framework thanks to a reduced hardware complexity enabled by the proposed method (a single coil for MRI, a few antennas for MWT and just phaseless measurements). Also, this is consistent with the ongoing integration of microwave hyperthermia systems with MRI scanners [36].

In this contribution, a two-dimensional configuration is considered. While this may be reasonable in the MRI case, a 3D model would be more appropriate for MWT. Moreover, the systems are herein modelled in terms of point sources embedded in an unbounded medium, whereas, for instance, MRI based tomography would require considering the presence of the RF shield of MRI scanner. In order to move the proposed technique to the stage of experimental/clinical validation, future work will therefore focus on the extension to 3D scenario, as well as on use of the Green's function in which the RF shield is included analytically or numerically. Also, the assessment of the MWT based EPs retrieval with existing microwave systems architectures (e.g. clinical devices used of hyperthermia) is in order.

Finally, further investigations will be devoted to the possibility of using of the proposed approach as a tool to quantitative monitor the physiological status of the tissues (and, so, the patients' health condition), and as wake-up calls about possible pathologies. In such a contest, innovative and unconventional check-up and follow-up techniques could be introduced.

Appendix

In this section, the expressions of the gradient and the line search parameter related to the cost functional (7) in a CSI conjugate gradient scheme are reported.

Recalling that $\Delta\Phi_{\hat{\chi}} = \langle \nabla\Phi_{\hat{\chi}}, \Delta\hat{\chi} \rangle$ and $\Delta\Phi_W = \langle \nabla\Phi_W, \Delta W \rangle$, and denoting with $\mathcal{T}^{-1}$ the inverse operator which transforms the tissue space coefficients into a pixel contrast, the gradients with respect to W and $\hat{\chi}$ of the cost functional are given by [14]:

$$\nabla\Phi_{\hat{\chi}} = 2 \sum_\nu \frac{\mathcal{T}^{-1}[(E_i + \mathcal{A}_i[W])^* \, m_s]}{\eta_S}$$

$$\nabla\Phi_W = 4 \frac{\mathcal{A}^+[(\mathcal{A}[W] + F_i) \, m_D]}{\eta_D} + 2 \frac{\mathcal{A}_i^+[\chi^* m_s] - m_s}{\eta_S}$$

(A.1)

where $m_S = \mathcal{T}(\hat{\chi})E_i + \mathcal{T}(\hat{\chi})\mathcal{A}_i[W] - W$ and $m_D = |\mathcal{A}[W] + F_i|^2 - M_t^2$ represents the misfit about the state and data equation, respectively, and the superscripts $*$ and $+$ denote the complex conjugate and the adjoint operations, respectively. Accordingly, the line minimization step μ_k is performed as:

$$\mu_k = \arg\min \Phi(\chi_k + \mu_k\Delta\chi_k, W_k + \mu_k\Delta W_k)$$
$$= \arg\min (a\lambda^4 + b\lambda^3 + c\lambda^2 + d\lambda + e)$$

(A.2)

where $\Delta\chi_k$ and ΔW_k represent the descent research directions considered at the *k*th iteration. Due to the nature of the involved operators, this latter can be rewritten as a fourth-degree algebraic polynomial with coefficients:

$$a = \sum_\nu \frac{\|\mathcal{T}(\Delta\hat{\chi})\mathcal{A}_i[\Delta W]\|^2}{\eta_S} + \sum_\nu \frac{\||\mathcal{A}[\Delta W]|^2\|_{l_2}^2}{\eta_D}$$

$$b = 2\mathcal{R}e \sum_\nu \frac{\langle \mathcal{T}(\Delta\hat{\chi})\mathcal{A}_i[\Delta W], \Delta m_S \rangle}{\eta_S} +$$
$$+ 2 \sum_\nu \frac{\langle |\mathcal{A}[\Delta W]|^2, \Delta m_D \rangle}{\eta_D}$$

$$c = \sum_\nu \frac{\|\Delta m_s\|^2}{\eta_S} + 2\mathcal{R}e \sum_\nu \frac{\langle \mathcal{T}(\Delta\hat{\chi})\mathcal{A}_i[\Delta W], m_S \rangle}{\eta_S} +$$
$$+ \sum_\nu \frac{\|\Delta m_D\|^2}{\eta_D} + 2\mathcal{R}e \sum_\nu \frac{\langle |\mathcal{A}[\Delta W]|^2, m_D \rangle}{\eta_D}$$

$$d = 2\mathcal{R}e \sum_\nu \frac{\langle m_S, \Delta m_S \rangle}{\eta_S} + 2\mathcal{R}e \sum_\nu \frac{\langle m_D, \Delta m_D \rangle}{\eta_D}$$

$$e = \sum_\nu \frac{\|m_s\|^2}{\eta_S} + \sum_\nu \frac{\|m_D\|^2}{\eta_D}$$

(A.3)

where $\Delta m_S = \mathcal{T}(\Delta\hat{\chi})(E_i + \mathcal{A}_i[W]) + \mathcal{T}(\hat{\chi})\mathcal{A}_i[\Delta W] - \Delta W$, $\Delta m_D = 2\mathcal{R}e\langle \mathcal{A}[W] + F_i, \mathcal{A}[\Delta W] \rangle$ and $\mathcal{R}e(\cdot)$ extracts the real part of the argument.
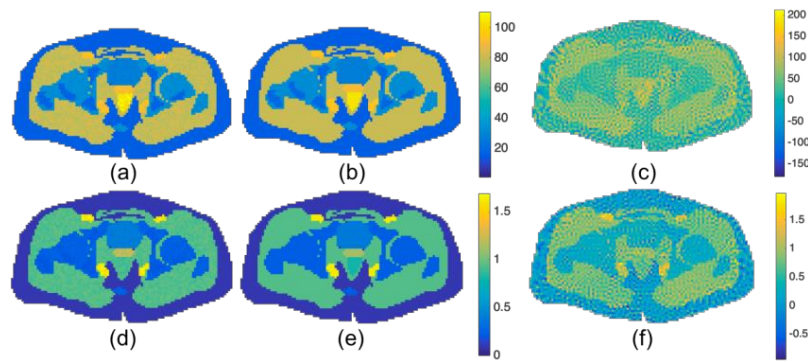
Figure 1. *In-vivo* EPs estimation by processing MRI data: Reference (a)-(d) and retrieved permittivity and conductivity profiles for the pelvis scenario respectively with $\mathcal{T}_n$ basis (b)-(e) and pixel basis (c)-(f) (SNR = 40dB).
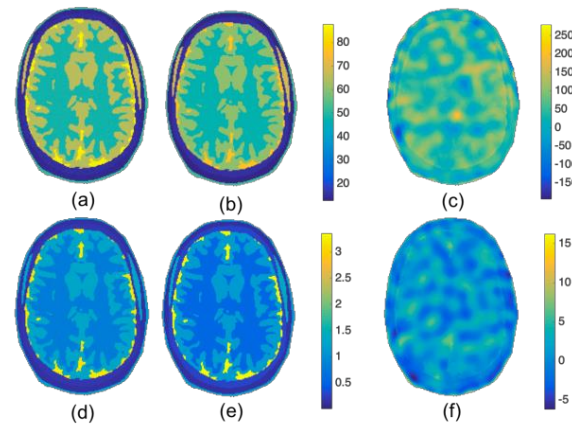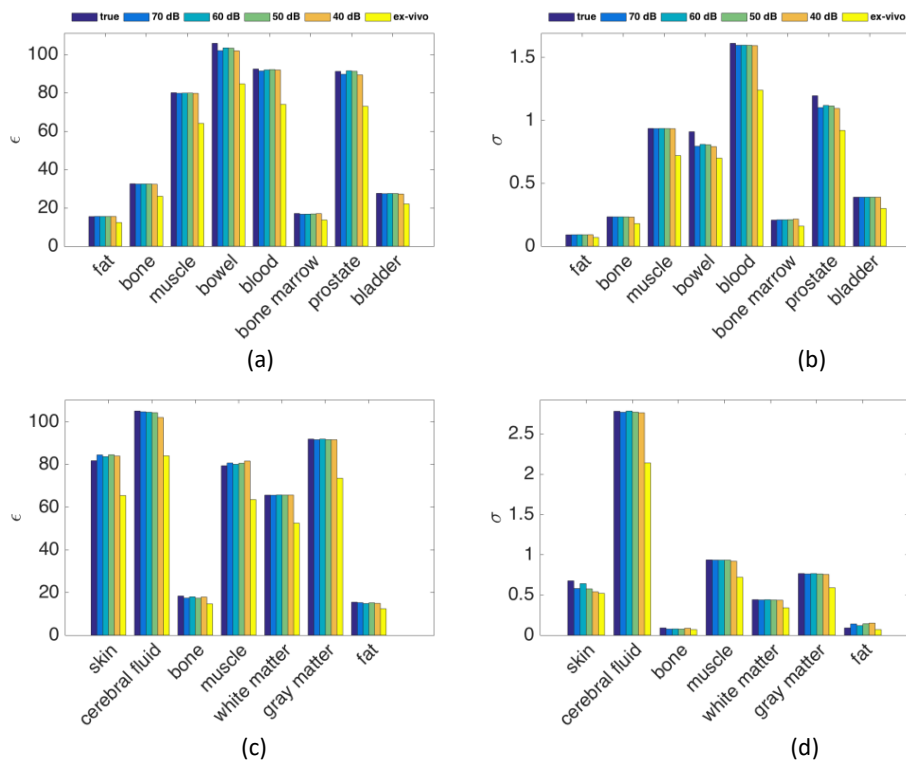

Figure 2. *In-vivo* EPs estimation by processing MWT data: Reference (a)-(d) and retrieved permittivity and conductivity profiles for the head scenario respectively with $\mathcal{T}_n$ basis (b)-(e) and pixel basis (c)-(f) (SNR = 40dB and N_A=32).

Figure 3. *In-vivo* EPs estimation by processing MRI data: Retrieved values of permittivity and conductivity corresponding to the **abdomen** (a-b) and the **head** (c-d).
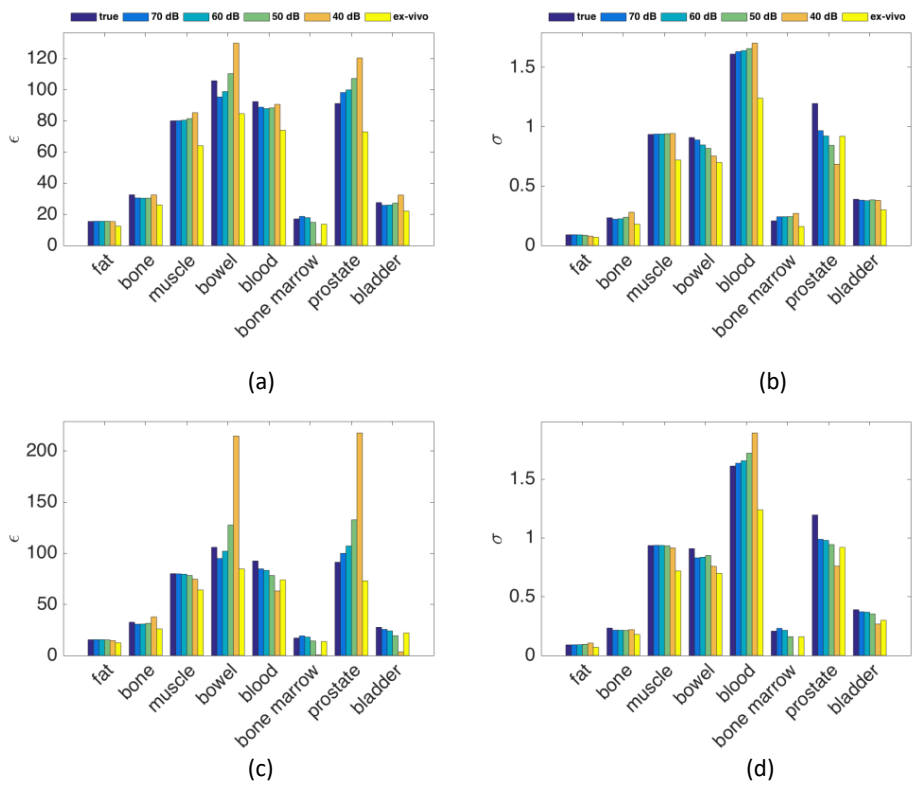
Figure 4. *In-vivo* **EPs estimation by processing MWT data**: Retrieved values of permittivity and conductivity of **pelvis** tissues corresponding to N_A=34 (a)-(b) and N_A=20 (c)-(d).
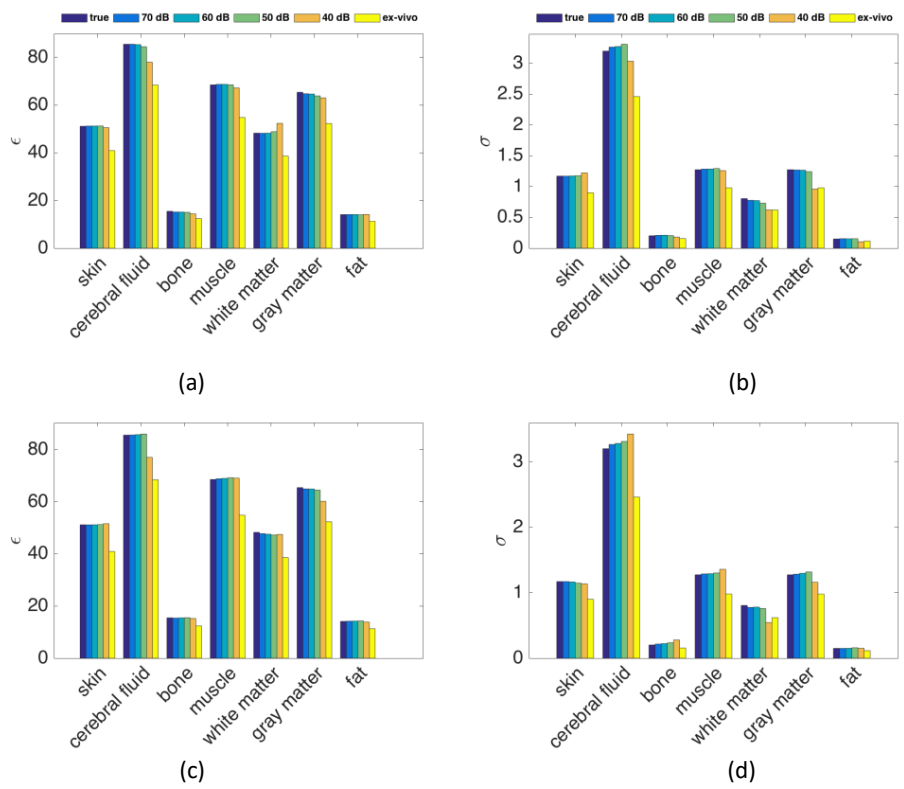

Figure 5. *In-vivo* **EPs estimation by processing MWT data**: Retrieved values of permittivity and conductivity of **head** tissues corresponding to N_A=44 (a)-(b) and N_A=32 (c)-(d).

Note that differently from [17] wherein an arbitrary number of iterations is considered, the adopted stopping rule is based on the change of the cost functional in successive iterations. If this difference between two successive iterations is lower than a threshold, the conjugate gradient-based minimization procedure stops.

An important consideration in solving the problem (7) via a conjugate gradient scheme is that χ and W may vary greatly in magnitude. For this reason, in this paper, we rescale these two variables according to [37].

Acknowledgements

References

[1] Rijnen et al., Quality and comfort in head and neck hyperthermia: A redesign according to clinical experience and simulation studies, *Int J Hyperthermia*, 31(8): 823–830, 2017.

[2] G.G. Bellizzi, D.A.M. Iero, L. Crocco, T. Isernia, Three-Dimensional Field Intensity Shaping: The Scalar Case, *IEEE Antennas and Wireless Propagation Letters*, 17 (3), 360-363,2018.

[3] G.G. Bellizzi, L. Crocco, G.M. Battaglia, T. Isernia, Multi-Frequency Constrained SAR Focusing for Patient Specific Hyperthermia Treatment, *IEEE Journal of Electromagnetics, RF and Microwaves in Medicine and Biology*, 1(2): 74-80, 2017.

[4] Durney, C H., Electromagnetic dosimetry for models of humans and animals: A review of theoretical and numerical techniques, *Proceedings of the IEEE*, 68(1): 33-40, 1980.

[5] S. Gabriel, R W Lau, C. Gabriel, The dielectric properties of biological tissues: II. Measurements in the frequency range 10 Hz to 20 GHz, *Phys. Med. Biol.*, 41: 2251-2269, 1996.

[6] R J Halter et al, The correlation of in-vivo and ex-vivo tissue dielectric properties to validate electromagnetic breast imaging: initial clinical experience, *Physiol. Meas*. 30(6): S121, 2009.

[7] E. M. Haacke, L. S. Petropoulos, E. W. Nilges, D. H. Wu, Extraction of conductivity and permittivity using magnetic resonance imaging, *Phys. Med. Biol.*, 36: 723-34, 1991.

[8] U. Katscher, C. A. Berg, Electric properties tomography: Biochemical, physical and technical background, evaluation and clinical applications, *NMR in Biomedicine*, 2017.

[9] R. Hong et al., 3-D MRI-Based Electrical Properties Tomography Using the Volume Integral Equation Method, *IEEE Transactions on Microwave Theory and Techniques*, 65(12): 4802-4811, 2017.

[10] E. Balideman, C. A. van den Berg, J. Trinks, A. L. van Lier, A. J. Nederveen, L. J. Stalpers, H. Crezee, R. F. Remis, CSI-EPT: A Contrast Source Inversion Approach for Improved MRI-Based Electric Properties Tomography, *IEEE Trans. on Med. Imaging*, 34(9):1788-1796, 2015.

[11] X. Zhang, J. Liu and B. He, Magnetic-Resonance-Based Electrical Properties Tomography: A Review, *IEEE Reviews in Biomedical Engineering*, 7:87-96, 2014.

[12] D. Colton and R. Kress. Inverse Acoustic and Electromagnetic Scattering Theory, Springer-Verlag, Berlin, Germany, 1998.

[13] I. Saniour, G. Gaborit, A. L. Perrier et al, Electro-optic probe for real-time assessments of RF electric field produced in an MRI scanner: feasibility tests at 3 and 4.7 T, *NMR in Biomedicine*, 31(1):e3849, 2018.

[14] M. D'Urso, K. Belkebir, L. Crocco, T. Isernia, and A. Litman, Phaseless imaging with experimental data: facts and challenges, *J. Opt. Soc. Am. A*, 25(1): 271-281, 2008.

[15] P. M. van den Berg and R. E. Kleinman, A contrast source inversion method, *Inv. Prob.*, 13:1607–1620, 1997.

[16] A. Golnabi et al., 3D microwave tomography of the breast using prior anatomical information, *Med Phys*., 43(4): 1933–1944, 2016.

[17] A. Arduino, O. Bottasuscio, M. Chiampi, L. Zilberti, Magnetic resonance-based imaging of human electric properties with phaseless contrast source inversion, *Inv. Probl.*, 34(8): 084002, 2018.

[18] P. Meaney et al., Integration of microwave tomography with magnetic resonance for improved breast imaging, *Med Phys,* 40(10), 2013.

[19] L. M. Neira et al., High-resolution microwave breast imaging using a 3-D inverse scattering algorithm with a variable-strength spatial prior constraint, *IEEE Trans. Antennas Propag.* 65(11):6002-6014, 2017.

[20] A. Rahimov, A. Litman and G. Ferrand, MRI-based electric properties tomography with a quasi-Newton approach, Inverse Problems 33(10), 2017.

[21] J. Liu, X. Zhang, P. F. van de Moortele, S. Schmitter, and B. He, Determining electrical properties based on B1 fields measured in an MR scanner using a multi-channel transmit/receive coil: A general approach, *Phys. Med. Biol.*, 58: 4395–4408, 2013.

[22] K. Setsompop, L. L. Wald, V. Alagappan, B. Gagoski, F. Hebrank, U. Fontius, F. Schmitt, E. Adalsteinsson, Parallel RF transmission with eight channels at 3 Tesla, *Magn. Reson. Med.*, 56: 1163-1171, 2006.

[23] P. Vernickel, P. Röschmann, C. Findeklee, C. Lüdeke, C. Leussler, J. Overweg, U. Katscher, I. Grässlin, K. Schünemann, Eight-channel transmit/receive body MRI coil at 3T. *Magn. Reson. Med.*, 58: 381-389, 2007.

[24] M. Bevacqua, L. Crocco, T. Isernia, "Non-linear Inverse Scattering via Sparsity Regularized Contrast Source Inversion", *IEEE Transactions on Computational Imaging*, 3(2): 296-304, June 2017.

[25] R. Palmeri, M. T. Bevacqua, L. Crocco, T. Isernia and L. Di Donato, Microwave Imaging via Distorted Iterated Virtual Experiments, in *IEEE Trans. on Antennas and Prop.*, 65(2): pp. 829-838, 2017.

[26] T. Isernia, V. Pascazio and R. Pierri, On the local minima in a tomographic imaging technique, *IEEE Trans. on Geosci. and Remote Sens.*, 39(7): 1596-1607, Jul 2001.

[27] J. Crezee, P. M. A. Van Haaren, H. Westendorp, M. De Greef, H. P. Kok, J. Wiersma, G. Van Stam, J. Sijbrands, P. Zum Vrde Sive Vrding, J. D. P. Van Dijk, M. C. C. M. Hul- shof, and A. Bel, Improving locoregional hyperthermia delivery using the 3-d controlled amc-8 phased array hyperthermia system: a

preclinical study, International journal of hyperthermia, 25: 581–592, Nov. 2009.

[28]   M. M. Paulides, G. M. Verduijn, and N. Van Holthe, Status quo and directions in deep head and neck hyperthermia, *Radiat Oncol*, 11(1): 21, 2016.

[29]   I. Zubal, C. Harrell, E. Smith, Z. Rattner, G. Gindi, and P. Hoffer, Computerized three-dimensional segmented human anatomy, *Med. Phys.*, 21(2): 299–302, 1994.

[30]   P. A. Hasgall, F. D. Gennaro, C. Baumgartner, E. Neufeld, M. Gosselin, D. Payne, A. Klingenbock, and N. Kuster, IT'IS Database for thermal and electromagnetic parameters of biological tissues, Version 3.0, 2015.

[31]   S. Salahuddin, A. La Gioia, M. A. Elahi, E. Porter, M. O'Halloran, A. Shahzad, Comparison of in-vivo and ex-vivo dielectric properties of biological tissues, *International Conference on Electromagnetics in Advanced Applications*, Verona, pp. 582-585, 2017.

[32]   O'Rourke, A. P., Lazebnik, M., Bertram, J. M., Converse, M. C., Hagness, S. C., Webster, J. G., & Mahvi, D. M., Dielectric properties of human normal, malignant and cirrhotic liver tissue: in-vivo and ex-vivo measurements from 0.5 to 20 GHz using a precision open-ended coaxial probe, *Phys. Med. Biol.*, 52: 4707–19, 2007.

[33]   R. Scapaticci, L. Di Donato, I. Catapano, and L. Crocco, A feasibility study on microwave imaging for brain stroke monitoring, *Progress In Electromagnetics Research B*, 40: 305-324, 2012.

[34]   R. Scapaticci, M. Bjelogrlic, J. A. T. Vasquez, F. Vipiana, M. Mattes, L. Crocco, Microwave Technology for Brain Imaging and Monitoring: Physical Foundations, Potential and Limitations, in *Emerging Electromagnetic Technologies for Brain Diseases Diagnostics, Monitoring and Therapy*, pp. 7-35, *Springer, Cham*, 2018.

[35]   P. H. Tournier, P. H., Bonazzoli, M., Dolean, V., Rapetti, F., Hecht, F., Nataf, F., Aliferis, I., El Kanfoud, I., Migliaccio, C., de Buhan, M, et al., Numerical Modeling and High-Speed Parallel Computing: New Perspectives on Tomographic Microwave Imaging for Brain Stroke Detection and Monitoring., *IEEE Ant. Prop. Magazine*, 59(5): 98-110, Oct. 2017.

[36]   J. Gellermann, W. Wlodarczyk, A. Feussner, H. Fähling, J. Nadobny, B. Hildebrandt, R. Felix, P. Wust, Methods end potentials of magnetic resonance imaging for monitoring radiofrequency hyperthermia in a hybrid system, *Int J Hyperthermia*, 21(6): 497–513, 2005.

[37]   John E. Dennis and Robert B. Schnabel, Numerical methods for unconstrained optimization and nonlinear equations, vol. 16, chap. 7. *Siam*, 1996.